Supersonic Propulsive Divert Maneuvers for Future Robotic and Human Mars Missions

Author:
Amit B. Mandalia

Advisor:
Prof. Robert D. Braun

December 13, 2013

Supersonic Propulsive Divert Maneuvers for Future Robotic and Human Mars Missions

Amit B. Mandalia[1] and Robert D. Braun[2]
Georgia Institute of Technology, Atlanta, Georgia, 30332

Future robotic and human missions to Mars require improved landed precision and increased payload mass. Two architectures that seek to meet these requirements using supersonic propulsive diverts are proposed in this paper: one utilizing a high-altitude propulsive divert and another with thrust vectoring during supersonic retropropulsion. Low ballistic coefficient entry vehicles decelerate high in the thin Mars atmosphere and may be used to deliver higher-mass payloads to the surface. A high-altitude supersonic propulsive divert maneuver is proposed as a means of precision landing for low ballistic coefficient entry vehicles that decelerate to supersonic speeds at altitudes of 20-60 km. This divert maneuver compares favorably to traditional precision landing architectures with up to 100% improvement in range capability while saving over 30% in propellant mass. Architectures which utilize hypersonic vehicles with ballistic coefficients of 10 kg/m^2 were found to land within 500 m of a target with this maneuver alone. This high-altitude divert range capability is sensitive to altitude and flight-path angle variations at maneuver initiation and relatively insensitive to velocity at initiation. Propellant mass fraction is relatively invariant to the initial conditions and correlates directly with the divert distance. Supersonic retropropulsion has also been proposed as a means to deliver higher-mass payloads to the surface, and thrust vectoring during supersonic retropropulsion can save a substantial amount of fuel in a precision landing scenario. Propellant mass savings greater than 30% are possible if thrust vectoring is unconstrained during the supersonic phase of flight. Propellant mass fraction is found to be sensitive to the divert direction and also the altitude and flight-path angle, favoring low altitudes and shallow flight-path angles.

Nomenclature

A	=	Axial force
β	=	Ballistic coefficient, kg/m^2
C	=	Aerodynamic coefficient
CI	=	Confidence Interval
ΔV	=	Change in velocity, m/s
D	=	Diameter, m
DoF	=	Degree-of-freedom
γ	=	Flight-path angle, defined as positive above the horizon, °
h_0	=	Initial altitude, km
L/D	=	Lift-to-drag ratio
m_0	=	Initial mass, kg
m_{prop}	=	Propellant mass, kg
N	=	Normal Force
s	=	Range, m
θ	=	Off-velocity thrust angle, °
T/W	=	Thrust to Weight, referenced to Mars
V	=	Velocity, m/s

[1] Graduate Research Assistant, Guggenheim School of Aerospace Engineering, AIAA Student Member, a.mandalia@gatech.edu

[2] David and Andrew Lewis Professor of Space Technology, Guggenheim School of Aerospace Engineering, AIAA Fellow, robert.braun@ae.gatech.edu

I. Introduction

FUTURE Mars missions will require improved landed accuracy to safely access areas of scientific interest and strategically place infrastructure for human missions. Also, to increase scientific return and potentially land humans on Mars, larger landed masses are required.[1] Large masses are difficult to land on Mars due to the thin atmosphere which limits aerodynamic deceleration during entry, descent, and landing (EDL). Improved accuracy and landed mass at Mars have received significant attention in the past 10 years.[2,3] Inflatable aerodynamic decelerators (IADs) can allow for greater landed mass and supersonic retropropulsion (SRP) has been shown to be an enabling technology for human missions.[4] Current efforts to increase landed accuracy are focused on hypersonic entry and propulsive terminal descent. Guided hypersonic entry, which was successfully demonstrated at Mars for the first time on the Mars Science Laboratory (MSL) mission in 2012,[5] improved landing accuracy substantially in comparison to previous missions. Future landing architectures further propose landing accuracy improvements by employing fuel-optimal algorithms[6] for propulsive descent from the end of parachute flight to a targeted landing site.[7] The state-of-the-art EDL architecture at Mars, with these elements, is shown in Figure 1.
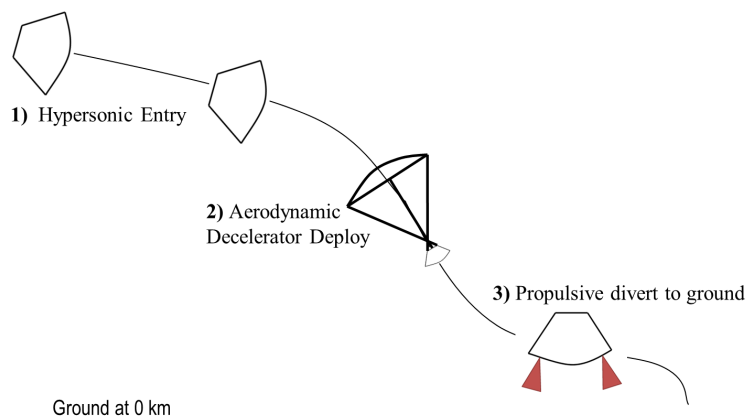

Figure 1. Traditional Entry, Descent, and Landing Architecture at Mars.

To increase the landed payload mass, it is paramount to ensure that the mass of propellant used is minimized. Fuel-optimal algorithms used during propulsive landing attempt to do this, but since these maneuvers are initiated at low altitudes, large diverts with shallow glideslopes require relatively large propellant mass fractions.[8] Beginning propulsive diverts earlier in the trajectory may reduce propellant usage and provide more altitude and timeline during landing.

Low ballistic coefficient vehicles, such as those that use hypersonic IADs (HIADs), have been shown to decelerate much higher in the atmosphere at Mars, between 20 and 60 km.[9] This allows for more time of flight between the end of hypersonic flight and the point of parachute deployment at 6-10 km. For the first part of this study, it is postulated that performing propulsive maneuvers during this high-altitude portion of flight to target a landing site will lead to an overall reduced propellant usage and a precision landing capability. By thrusting orthogonal to the velocity vector, all energy would be put into a divert to a target during the maneuver.

The second phase of the study explores the use of thrust vectoring during supersonic propulsive descent (supersonic retropropulsion) to accomplish a divert. Current SRP studies have evaluated thrusting directly opposite the velocity,[4] but it is postulated that thrust vectoring can allow for efficient fuel use in a precision landing scenario. Like the architecture described above, the higher velocities and altitude of such a maneuver might allow for greater diverts at decreased propellant costs relative to a divert that begins during subsonic flight. Table 1 summarizes guidance techniques that can be used to decrease landing error at Mars, where the shaded items are those investigated here. The proposed maneuvers fill a gap for crossrange control and downrange control during the descent phase of flight. Precision landing is defined by the mission requirements, as a human mission may require meter-level accuracy, while a science mission may require a 1 km accuracy, so the term will be used loosely as landing with some degree of targeting accuracy.

Table 1. Summary of in-flight precision landing techniques for Mars exploration missions.

	Deceleration Device	Crossrange control	Downrange control
Entry	Aeroshell (Rigid/Inflatable)	Bank-to-Steer	
Descent	Aerodynamic Decelerator (Rigid / Inflatable / Parachute)	Bank-to-Steer	
		None	Range Trigger
		Propulsive Divert Maneuver?	
	Supersonic Retropropulsion	Thrust Vector?	
Landing	Propulsive	Thrust Vector	
	Subsonic Parachute	Guided Parachute	
	Impact Attenuation	None	

II. Simulation Methods and Assumptions

A. Numerical Simulation

To perform high-fidelity simulations for the conceptual studies described in this paper, architectures were catalyzed through a three degree-of-freedom simulation. This simulation models the planet as a rotating oblate spheroid, and includes higher-order effects such as the J2 perturbation. The equations of motion are integrated with a constant timestep 4th order Runge-Kutta integration scheme in a planet-centered inertial frame. It is written in MATLAB, but autocoded to C to improve execution speed. Versions of this simulation have been validated and used in previous design studies.[10]

A simulated flight computer allows for the operation of navigation, guidance, and control at different rates. The simulation ends when the vehicle lands at the target altitude, initially set at 0 km. The simulation is run at a rate of 50 Hz, with guidance calls at 10 Hz.

B. Navigation Assumptions.

Perfect navigation (full state knowledge) is assumed for this simulation. Traditional Mars missions use an inertial navigation system with radar altimetry for altitude updates to a navigation filter. For MSL, which used such a navigation approach, the difference between the onboard navigated landing location and the actual landing location was 162 m.[11] Depending on the mission requirements, this may be adequate, however, other sensors can be used if improved navigation knowledge is required.

Terrain-relative navigation (TRN) can decrease position knowledge error to 20 m,[12] and the discussed architectures can allow for accommodation of a TRN camera. For the high-altitude divert architecture, a camera can be exposed after the jettison of the low ballistic coefficient vehicle. In the process of exposing the engines for supersonic retropropulsion, a camera sensor can also be exposed for terrain viewing. It is likely that position knowledge error will increase at higher altitudes and velocities, but as altitude decreases, the estimates will become more accurate. Radiometric navigation can also be used to improve state estimates in real-time, through the use of orbital or ground beacons.[13] Orbiting beacons may be available once enough orbiting assets are placed around Mars, and ground beacons may be used in cases where existing infrastructure exists on the surface of Mars, like would be the case with Mars Sample Return or a human mission. Since the maneuvers occur below Mach 5, ionized flow that may attenuate radio signals is unlikely to exist in the bow shock.

C. Planetary Models

Atmospheres are generated using Mars-GRAM 2010,[14] and correspond to an August 6, 2012 landing date (MSL's landing date) using default Mars-GRAM settings. A dust tau of 0.3 was used for these atmospheres. A nominal atmosphere without winds is used for the nominal performance and sensitivity analysis. For the Monte Carlo analyses, a set of 1000 dispersed atmospheres with winds are generated. This landing date corresponds to a time when the Mars atmosphere is at the lower half of its pressure cycle, thereby representing a conservative set of atmospheres in comparison to other times of the Martian year. Other parameters used to characterize Mars in the simulation are found in Table 2.

Table 2. Properties of Mars.

Property	Value
Equatorial Radius	3396.2 km
Polar Radius	3376.2 km
Gravitational Parameter, μ	4.283×10^{13} m^3 / s^2
J2 Perturbation	1.9605×10^{-3}
Ratio of Specific Heats	1.294
Sutton-Graves Coefficient	1.898×10^{-4} kg$^{0.5}$/m

D. Vehicle Models

Aerodynamic models are used for the aeroshell and the parachute. A MSL-class 3300 kg vehicle is modeled, with a 4.5-m diameter 70° sphere-cone forebody with a nose radius of 1.125 m. Only C_A and C_N are modeled, with bank angle tracked to point the lift vector in the correct direction. For an MSL lifting entry at α_{tot} = -16° and ballistic α_{tot} = 0°, an existing aerodynamic database was used. A disk-gap-band parachute with D_o = 19.7 m was used in the simulations, using a historical aerodynamic database.[15]

Engines are modeled as force vectors that can point in any direction, restricted by minimum and maximum thrust magnitudes. Restrictions on the thrust pointing are specific to the configurations conceptualized below. Hydrazine thrusters (Isp = 225 s) were used for the high-altitude divert maneuver study and methane-LOx engines (Isp = 350 s) were used for the SRP study.

E. Entry State

An MSL-like entry state[9] was used unless otherwise stated. This allowed for parity to compare results and also make sure realistic dispersions were used. The target was always at an altitude of 0 km and the latitude/longitude of the target depended on the scenario.

Table 3. Entry state for simulations.

Entry State	Value
Inertial Flight-Path Angle, γ	-15.5°
Inertial Entry Velocity	6.1 km/s
Azimuth	90°
Entry Interface (EI) Altitude	135 km
EI Latitude	0°
EI Longitude	0°

F. Monte Carlo Dispersions

The dispersions used in the Monte Carlo Simulation are found in Table 4, along with their references. Entry state delivery errors are correlated from a MSL delivery covariance matrix.[9]

Table 4. Monte Carlo Dispersions

	Parameter	Dispersion, Min/Max or 3σ	Reference
Entry State	Inertial Flight-Path Angle, γ	0.05°	Gaussian, Ref. 9
	Inertial Entry Velocity	2.0 m/s	Gaussian, Ref. 9
	Azimuth	0.005°	Gaussian, Ref. 9
	Entry Interface (EI) Altitude	2.5 km	Gaussian, Ref. 9
	EI Latitude	0.1°	Gaussian, Ref. 9
	EI Longitude	0.1°	Gaussian, Ref. 9
	Vehicle mass	3.0 kg	Gaussian, Ref. 9
Vehicle	Hypersonic C_A	3%	Uniform, Ref. 16
	Hypersonic C_N	10%	Uniform, Ref. 16
	Supersonic C_A	5%	Uniform, Ref. 16
	Supersonic C_N	8%	Uniform, Ref. 16
	Parachute Aerodynamics	From literature	Ref. 15
Planetary	Atmosphere	Generated in Mars-GRAM	Described above

III. High-Altitude Divert Architecture

A. Conceptual Description

The high-altitude divert maneuver can be thought of as a modification to powered descent. Typical powered descent methods use a single thrust vector to provide both deceleration and divert capabilities. The idea behind the high-altitude divert maneuver is to still use terminal powered descent for deceleration and soft landing, but decouple the divert function and perform it earlier in the trajectory. It is postulated that this decoupling, accomplished by applying thrust normal to the velocity vector, can substantially reduce fuel usage. This thrust implementation allows for possible use of a lifting aerodynamic effector (in lieu of the thruster) and minimizes the total effect of the maneuver on the velocity to prevent excessive acceleration during maneuvers.

B. Architecture Detail

The architecture that will be analyzed utilizes a hypersonic entry with a rigid heatshield or HIAD, a propulsive divert maneuver at high-altitudes, parachute flight for further deceleration, and a constant thrust propulsive gravity turn for a soft landing. The Mars-relative thrust-to-weight is constrained to be less than 0.5 in each direction (in-plane and out-of-plane) for the divert maneuver, and T/W = [2-5] (relative to Mars) for the gravity turn. A jettison Mach number for a given mission type is selected to ensure the nominal trajectory passes through the center of the parachute deployment box. Parachute deployment at 6-10 km allows for a relatively wide range of deploy conditions for a disk-gap-band (DGB) parachute on Mars, while still preserving altitude.[1] A propulsive gravity turn to the ground allows for the targeting performance of high-altitude divert maneuver to be examined with minimal external guidance influences. It also completes the decoupling of the propulsive maneuvers, where thrust for the gravity turn is only applied to decelerate the vehicle. Figure 2 shows this architecture in detail.
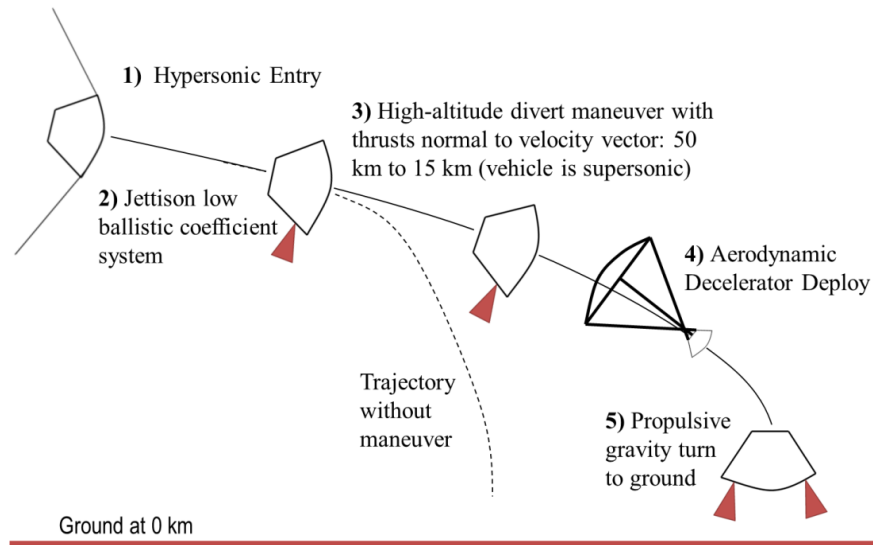

Figure 2. Architecture with high-altitude divert maneuver.

C. High-Altitude Divert Guidance

The guidance for the high-altitude divert maneuver consists of a closed-loop prediction-based algorithm. The algorithm propagates simplified equations of motion for the current trajectory to identify the vehicle's zero-effort landing location. The target is projected on the current plane of motion and compared to the zero-effort landing location to obtain the downrange miss distance. The magnitude of this projection off-the-plane allows for the calculation of the crossrange miss distance.

With knowledge of the miss distances, the thrust can be commanded to reach the target. As discussed earlier, the thrust is applied normal to the velocity vector. For downrange control, if vehicle is determined to be missing the target, thrust is commanded to force the vehicle to follow a trajectory toward a target in the current plane of motion. For crossrange control, thrust is commanded out-of-plane in the direction of the target. The closed loop implementation turns off the engine as soon as the predictor determines the zero-effort landing location converges on the target. This is described in further detail in Figure 3.
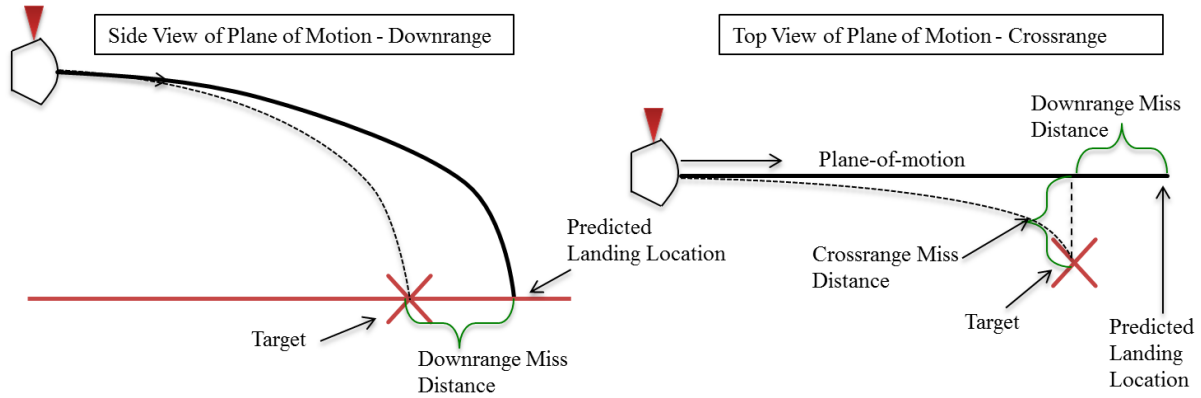
Figure 3. Description of high-altitude divert maneuver guidance strategy. In-plane thrusts are shown controlling downrange in the left image, and out-of-plane thrusts are shown controlling cross range in the right image.

D. Architecture Performance

1. Baseline Vehicle and Mission

To understand results of the maneuver, a modified Mars Science Laboratory (MSL)[17] vehicle was simulated. In order to accommodate this maneuver, pairs of Mars Landing Engines (MLEs) were spaced 90° apart on the plane normal to the velocity vector. This corresponds to a Mars-relative T/W = 0.5 in each channel. For the divert maneuver, the 3300 kg vehicle is assumed to be traveling at 0° angle-of-attack with the MLEs acting through the center of gravity. This configuration can be seen in Figure 4.
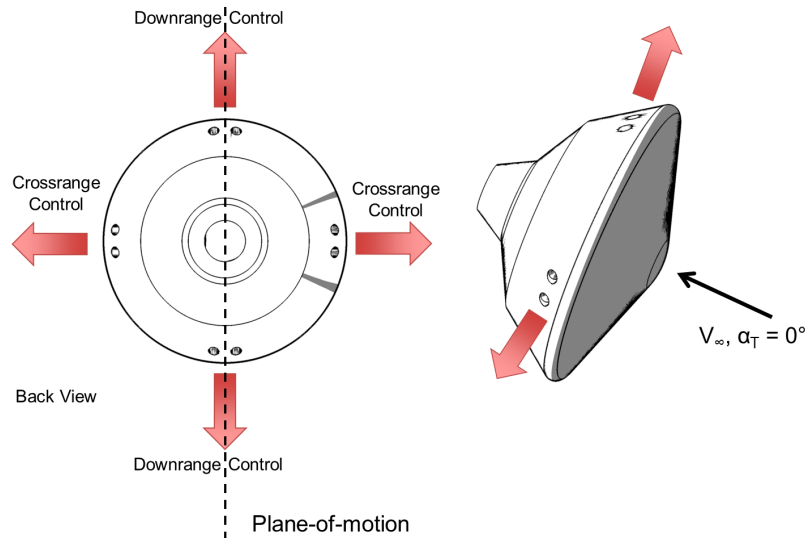
Figure 4. Configuration of vehicle with the high-altitude divert thrusters.

Vehicles with hypersonic ballistic coefficients of 1 kg/m^2, 5 kg/m^2, 10 kg/m^2, 20 kg/m^2, 50 kg/m^2, which enter ballistically, were simulated as part of this study, where ballistic coefficient is defined as m_{entry} / ($C_D A$). The hypersonic trajectories are based on the work of Meginnis et al.[9] The ballistic coefficients are varied with the addition of a HIAD to the system, whose mass is estimated using relationships from the literature.[18] The total entry mass is the mass of the HIAD plus 3300 kg. Table 5 lists the vehicle properties for the different vehicles. Trajectories are shown in Figure 5, where the hypersonic entry, high-altitude divert maneuver, flight on parachute, and propulsive gravity turn, are all modeled. The only mass changes modeled are HIAD jettison and propellant usage from propulsive maneuvering. At the point of HIAD jettison, the drag area is reduced to that of the MSL blunt body and the mass of the HIAD is subtracted. Also, if more precise navigation data is desired, a terrain-relative navigation (TRN) or radar sensor can be exposed during a jettison event.

Table 5. Low-β vehicle properties. Masses are estimated from known relationships.[18]

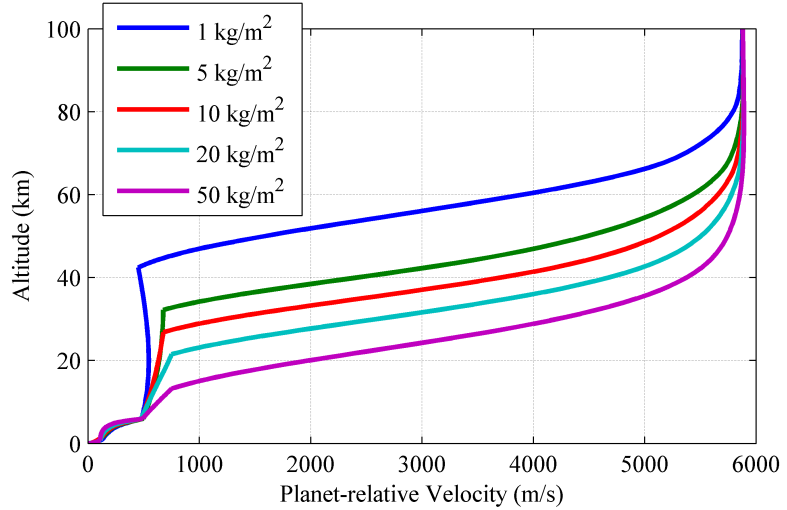| β (kg/m^2)	HIAD Diameter	HIAD Mass
1	56 m	500 kg
5	24 m	174 kg
10	17 m	83 kg
20	11.9 m	43 kg
50	7.5 m	27 kg

Figure 5. Low-β vehicle trajectories.

For all the trajectories, the jettison of the HIAD occurs at relatively low velocities. The jettison event appears as the discontinuity at 42 km, 33 km, 27 km, 22 km, and 16 km, for the 1 kg/m^2, 5 kg/m^2, 10 kg/m^2, 50 kg/m^2 trajectories in Figure 5, respectively. After that, a 3300 kg, β = 148 kg/m^2 vehicle at 0° angle-of-attack is released, and the divert maneuver is allowed to begin. For the 1 kg/m^2 case, the atmosphere is not dense enough at the high altitudes, so the vehicle initially accelerates, unlike the other trajectories, which continue decelerating after jettison. The jettison is commanded on a velocity trigger, and the velocities are chosen so that the post-jettison trajectory would fall through the center of the Disk-Gap-Band parachute deployment box. A range trigger may allow for further downrange control, but this would compete with this maneuver and was therefore not implemented. Mach, velocity, dynamic pressure at jettison, and maximum dynamic pressure for the nominal trajectories are found in Table 6. Jettison occurs after the dynamic pressure pulse, and since dynamic pressure at jettison is far lower than maximum dynamic pressure for the entire trajectory, it is likely that effects of aerodynamic and atmospheric uncertanties will be minimized.

Table 6. Nominal trajectory parameters at jettison, including maximum dynamic pressure.

β (kg/m^2)	Jettison Velocity (m/s)	Mach Number at Jettison	Dynamic Pressure at Jettison (Pa)	Maximum Dynamic Pressure (Pa)
1	450	2.406	12.98	180.8
5	675	3.491	122.4	754.5
10	675	3.381	229.2	1553
20	750	3.622	501.2	2979
50	750	3.417	1115	6780

Aerodynamic, wind, and atmospheric uncertainties are directly dealt with using thrust during the high-altitude divert maneuver, but after parachute deploy, these uncertainties act more strongly on the vehicle and there is no active guidance to prevent it's influence. It is anticipated that the greatest range error will be accumulated after parachute deployment.

2. Achievable Performance

From the nominal trajectories, Figure 6 shows how much range can be attained with such a maneuver (in terms of landed footprint), and at what propellant mass fraction for ballistic vehicles with ballistic coefficients of 1 kg/m^2, 5 kg/m^2, 10 kg/m^2, and 50 kg/m^2. The propellant mass fraction (PMF) is defined as PMF = m_{prop}/m_0, where m_0 is 3300 kg and m_{prop} is the total propellant used by the high-altitude divert and gravity turn. The attainable range corresponds to how much error can be cleaned up by the maneuver by performing a divert, and PMF inversely correlates with how much payload can be landed. The nominal target for the both maneuvers is at (0,0), and this was set based on the unguided landing site for the architectures.

To compare the results with current pinpoint landing architectures, state-of-the-art propulsive landing is simulated starting at Mach 0.8 to the ground for a soft landing at 0 km altitude for a standard MSL mission-type. A closed-form, analytic, acceleration-optimal guidance algorithm developed by D'Souza[19] is used as it is straight forward to implement and reflects the performance of other propulsive landing algorithms well.[8] The Mach 0.8 initiation showed a comparable range capability to the high-altitude divert maneuver, as compared to lower initiation Mach numbers.

A contoured map in Figure 6 is used to show the PMF of each of the architectures, with the maneuvers being symmetric in crossrange. A first observation is that the high-altitude divert maneuver uses substantially less propellant than the state-of-the-art propulsive landing architecture. It is evident that a large amount of propellant is necessary to decelerate from Mach 0.8 while diverting to a further location. For the state-of-the-art propulsive landing cases, the minimum PMF actually falls behind the (0,0) target due to the initial conditions of the maneuver, and the range achievable is limited by the T/W, which is set at 2 for this analysis (low in reality).
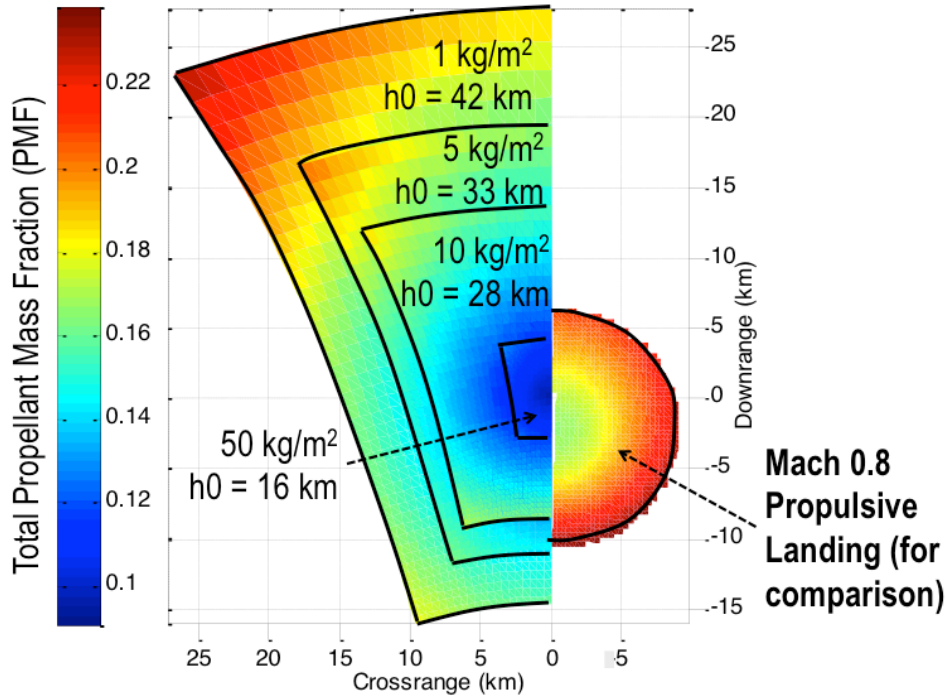

Figure 6. Ballistic entry downrange vs. crossrange (symmetric across crossrange, so only half shown) plotted with PMF contours for both the high-altitude divert maneuver architecture (left) and state-of-the-art propulsive landing (right).

The PMF contour does not change substantially across initiation altitudes, and is rather a function of range. The initial conditions do have a substantial influence on the shape of the achievable landed footprint. Higher initation altitudes allow the vehicle to travel considerably farther. Low initiation altitude limits the time available between maneuver start and parachute deployment, therefore restricting range achievable for the selected T/W. Positive downrange can be more easily achieved compared to negative downrange, since the thrust to travel positive downrange acts as a pseudo-lift, directly counteracting gravity. The thrust necessary to travel negative downrange causes the vehicle to lose considerable altitude and timeline to perform the maneuver.

3. Statistical Performance

Statistical performance of this maneuver is analyzed using a Monte Carlo simulation. One-thousand trajectories of $\beta \in \{1 \text{ kg/m}^2, 5 \text{ kg/m}^2, 10 \text{ kg/m}^2, 20 \text{ kg/m}^2, 50 \text{ kg/m}^2\}$ each with a gravity turn only (unguided), state-of-the-art propulsive landing initiated at Mach 0.8, and the high-altitude divert maneuver were run. The mean latitude and longitude of the gravity turn cases was set as the target for the state-of-the-art propulsive landing cases, while a target about 5 km further downrange was set for the high-altitude divert maneuver. Again, this takes advantage of the downrange divert capabilities seen in Figure 6. The results of these 15 sets of runs are seen in the following figures. In the cumulative probability density function for PMF (Figure 7), the high-altitude divert maneuver is 60-70% more expensive in PMF than the gravity turn by itself, while the state-of-the-art propulsive landing is upwards

of 200% more expensive. The state-of-the-art propulsive landing PMFs are not consistent through the cumulative distribution, since the result is highly sensitive to initial conditions, but the 99% CI PMF (between 0.27 and 0.32) is consistently higher than the other architectures.
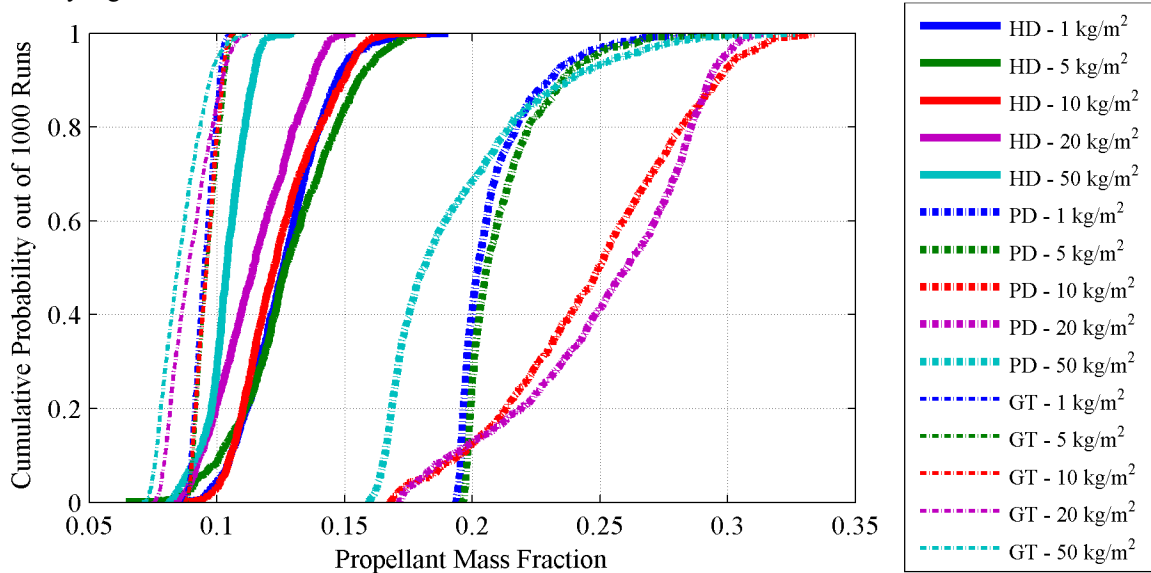

Figure 7. Cumulative Probability Function of PMF for all 15 architectures.

The 99% confidence level results for all the CDF's are summarized in Table 7. The results shaded in grey refer to mission types that were able to land within 500 m. The column PMF Reduction quantifies the percent difference between the high-altitude divert PMF and state-of-the-art propulsive landing PMF. Across all cases, the high-altitude divert maneuver uses at least 37% less propellant compared to the state-of-the-art propulsive landing case.

Table 7. 99% confidence statistics for Monte Carlo study.

β (kg/m^2)	Unguided (Gravity turn only): 99% CI		High-Altitude Divert Maneuver: 99% CI		State-of-the-art propulsive Landing: 99% CI		PMF Reduction
	PMF	Miss Distance (m)	PMF	Miss Distance (m)	PMF	Miss Distance (m)	
1	0.104	17000	0.173	201	0.278	0.7	-37.7%
5	0.106	14400	0.177	356	0.288	0.8	-38.5%
10	0.106	12000	0.164	494	0.328	39	-50%
20	0.111	13300	0.148	6200	0.310	57	-52.2%
50	0.111	15600	0.123	9800	0.301	11	-59.1%

Although the high-altitude divert maneuver's PMF performance is far better than state-of-the-art propulsive landings' PMF, the uncontrolled region past parachute deploy causes the vehicle to miss by several hundred meters for the most precise cases (Figure 8). This is compared to state-of-the-art propulsive landing, which is able to land within a few meters of the target. If a 500 m miss distance is deemed to be acceptable for a mission, it can be said that high-altitude divert architectures of this type with $\beta \leq 10$ kg/m^2 should be able to achieve this landing requirement, possibly without the need for entry guidance. Targeting performance drops when $\beta \geq 20$ kg/m^2, as altitude and timeline to perform the divert maneuver decrease at the higher ballistic coefficients.
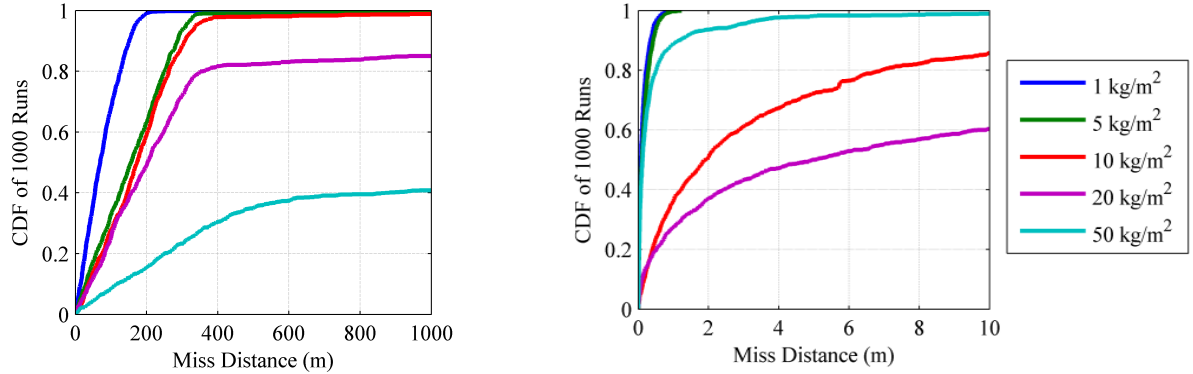
Figure 8. CDF's of miss distance for the high-altitude divert (left) and the state-of-the-art propulsive landing (right).

Each of the 1000 trajectories for the β = 5 kg/m^2 mission are shown in Figure 9. For the high-altitude divert, downrange error is clearly decreased during the high-altitude maneuver, while the state-of-the-art propulsive landing waits until the last few km of altitude to begin a large divert (often over 10 km). It was postulated that there were PMF advantages to starting a divert at higher altitudes compared to a shallow glideslope state-of-the-art propulsive landing, and this is confirmed by the results in Table 7.
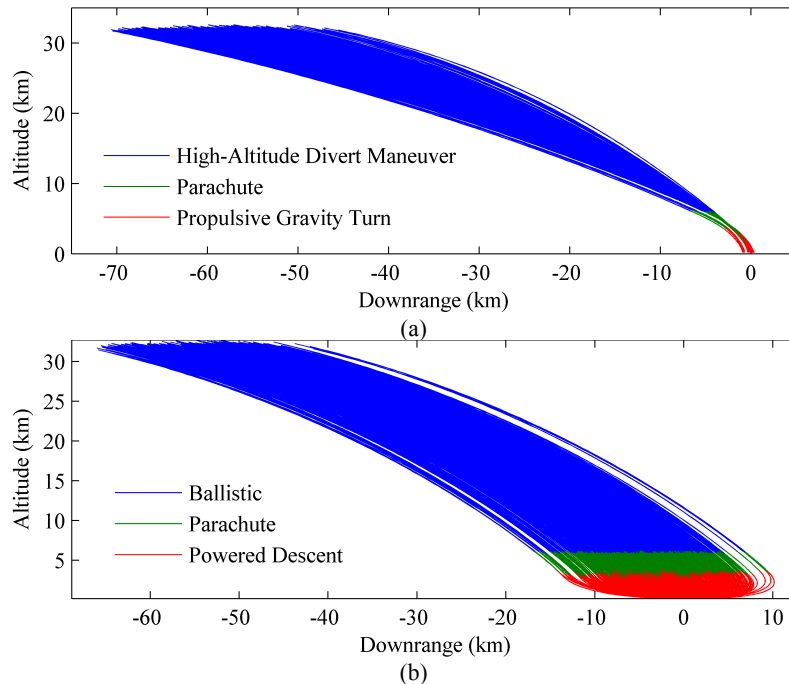
Figure 9. Altitude verse downrange for the high-altitude divert architecture (a) and optimal powered descent (b)

A plot of the 1000 crossrange verse downrange trajectories for the high-altitude divert maneuver (β = 5 kg/m^2 mission) can be found in Figure 10. The heading change for all trajectories happens quickly, soon after the initiation of the divert maneuver and far uprange (over 40 km) away from the target. Likewise, the maneuver is able to control crossrange on the order of meters. This is in comparison to the crossrange verse downrange trajectories for the state-of-the-art propulsive landing architecture, shown in Figure 11, where powered descent flight is shown (the only precision guided part of flight). The initial crossrange error is increased in comparison to the high-altitude divert, as the propulsive landing divert starts at a lower altitude allowing aerodynamic and wind uncertainties to have more opportunity to act on the vehicle. However, the state-of-the-art propulsive landing is capable in reducing the range error, including the downrange error seen in Figure 9, down to 0.8 m at 99% CI (Table 8).
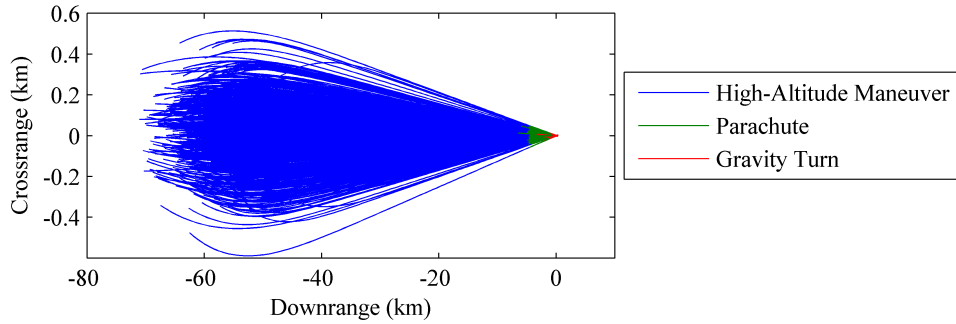
Figure 10. Crossrange verse downrange for the high-altitude divert maneuver.
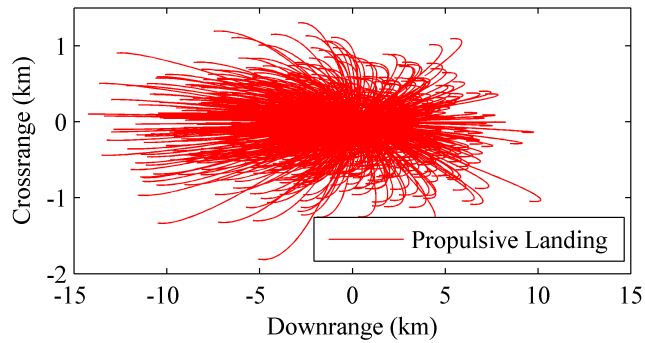

Figure 11. Crossrange verse downrange for the state-of-the-art propulsive landing (only powered descent flight is shown).

To get a better idea of the as-landed performance of the architectures, the touchdown locations for the 1000 samples from the Monte Carlo simulations of the $\beta = 5$ kg/m^2 mission are reported in Figure 12. Note that the high-altitude divert maneuver's landed positions are further downrange than the state-of-the-art propulsive landing target since it's target is further downrange. Compared to the unguided ellipse, the crossrange error is reduced to near zero when using the state-of-the-art propulsive landing and the high-altitude divert maneuver (indicated by almost no variation in crossrange). The high-altitude divert maneuver is also capable of reducing the downrange error by a factor of 10 compared to the unguided landing ellipse, while the state-of-the-art propulsive landing reduces downrange to near zero. The actual miss distances from the target for the $\beta = 5$ kg/m^2 missions are documented by the green CDF curves in Figure 8.
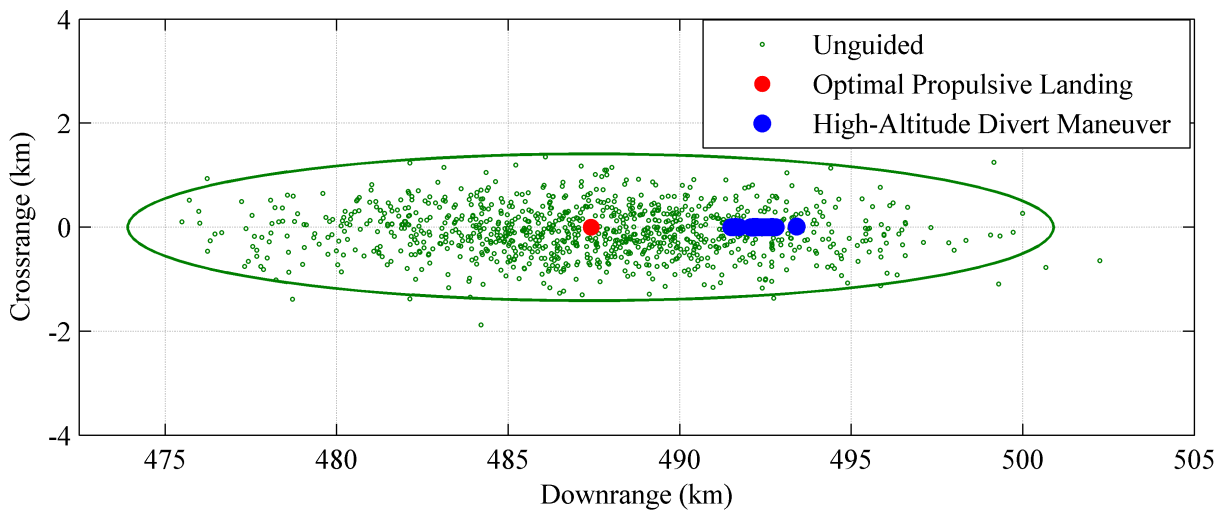

Figure 12. Touchdown locations for the $\beta = 5$ kg/m^2 architectures, with a landing ellipse drawn for the unguided cases. The touchdown locations at 0 km altitude of the 1000 sample Monte Carlo simulation are shown for each architecture.

11

E. Application to the Mars Science Laboratory Mission

MSL landed on Mars in August 2012, and used entry guidance to achieve its precision landing goals. A 148 kg/m^2, MSL vehicle with L/D = 0.24 is simulated and a modified Apollo Final Phase algorithm was used to target a landing site. One thousand Monte Carlo samples for the gravity turn only, state-of-the-art propulsive landing, and the high-altitude divert maneuver are run. The high-altitude divert is initated at a velocity of 750 m/s, to allow for timeline to perform the maneuver and pass through the parachute deployment box, at an altitude of about 18 km, while the other cases run hypersonic guidance until parachute deploy. Like before, the state-of-the-art propulsive landing target was chosen based on the mean latitude and longitude of the gravity turn runs, and the high-altitude divert maneuver target was chosen to be 5 km further downrange. The 99% confidence results are shown in Table 8. Although it was previously shown that $\beta > 10$ kg/m^2 are exhibit poor precision landing performance with a ballistic entry, the fact that the vehicle is lifting allows it to fly at shallow flight path angles that cover downrange quickly and also maintain altitude for longer periods of time. Likewise, guidance allows for improved downrange control, leading to considerably decreased total fuel use, with a PMF of 0.117 for the MSL application with high-altitude divert verse ~0.15 for the ballistic application.

Table 8. Performance summary of the architectures relative to a MSL mission.

Parameter	Gravity Turn Only: 99%	High-Altitude Divert Maneuver: 99%	State-of-the-art Propulsive Landing: 99%
PMF	0.087	0.117	0.212
Miss Distance	8.4 km	480 m	19 m

The same trends seen in the ballistic entries are seen here, with a landing within 480 m (at 99% CI) achievable at about half the propellant mass fraction of the state-of-the-art propulsive landing case.

F. System-Level Performance Sensitivities

Initial conditions and vehicle parameters are varied in the following sensitivity studies. A 3300 kg, 148 kg/m^2 ballistic 70° sphere-cone with 2 MLE's spaced 90° apart is simulated. Each trajectory also includes parachute deploy at around 6 km (altitude/velocity trigger) and a gravity turn to the ground for a soft landing. The sensitivity to altitude, flight-path angle, and velocity at initiation will be explored, representing possible terminal states of hypersonic entry with a variety of systems. For vehicle parameters, T/W correlates directly to engine selection on vehicles, so that will be explored, as well.

1. Altitude at Initiation

For a given entry state, the altitude at high-altitude divert initiation is driven by two main factors: the ballistic coefficient of the hypersonic entry vehicle and whether a lifting entry is used. Lower ballistic coefficients correspond to a higher altitude at initation and lifting entries can attain higher altitudes compared to ballistic entries for a given terminal velocity.[1] The sensitivity to initiation altitude is seen in Figure 13, where the independent variables are the initial altitude and velocity. The initiation velocity is chosen to ensure that the trajectory passes through the parachute deployment box. Results for three different flight angles are presented for a maximum positive downrange divert and a maximum crossrange divert. Both the downrange-only and maximum crossrange component demonstrate a relatively linear relationship. For this set of initial conditions, where velocity and flight path angle also play a role, about 10 km of range can be gained for every 10 km of increased initiation altitude. Increased altitude at initiation corresponds to increased time-of-flight, leading to increased divert distances and possibly explaining why greater crossrange is achievable compared to downrange at high initial altitudes.
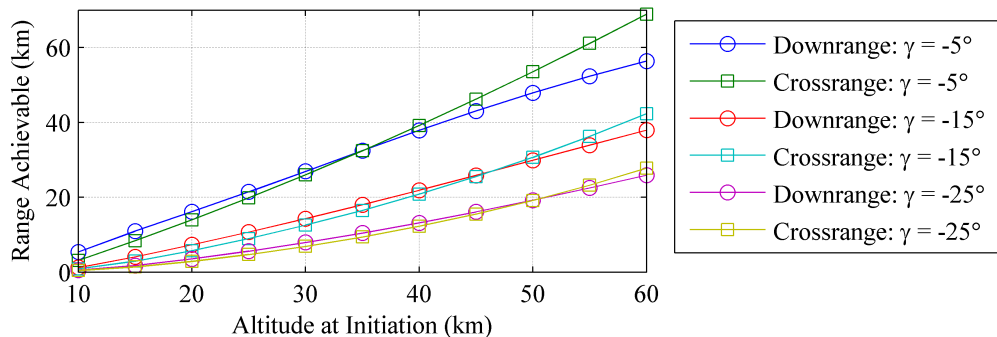

Figure 13. Range sensitivity to altitude at initiation of high-altitude divert maneuver.

2. Velocity at Initiation

Velocity at initiation and its sensitivity to divert range achievable is shown in Figure 14. The maximum positive downrange divert and maximum crossrange divert are shown. An initial altitude of 30 km was used for these cases, and the results for three flight-path angles at initiation are presented.
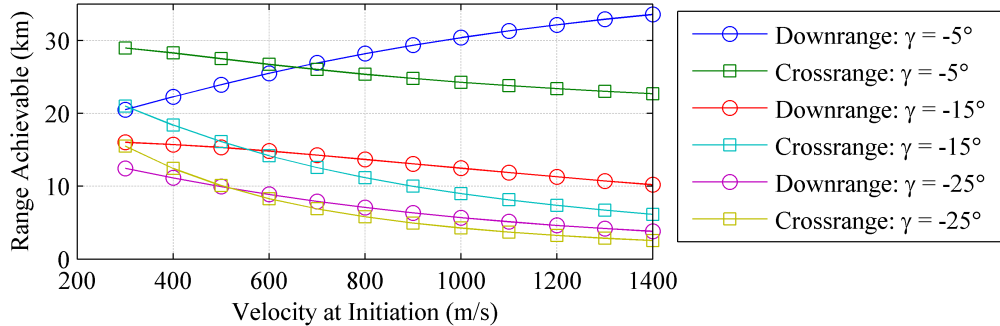

Figure 14. Range sensitivity to velocity and divert maneuver initiation.

Range achievable decreases with increased velocity and steeper flight path angles. This follows as the rate of decrease in altitude ($dh/dt = V \sin \gamma$) is larger in steep flight-path angle, high velocity situations. The $\gamma = -5°$ case does not follow this trend in downrange, likely due to the divert maneuver allowing the vehicle to maintain altitude more easily at this shallow flight-path angle and allowing the vehicle to travel further downrange ($ds/dt = V \cos \gamma$).

3. Flight-path Angle at Initiation

For the flight-path angle sensitivity, planet-relative velocity at initiation was fixed at 800 m/s, and flight-path angle was swept from -5° to 50°. Three different initiation altitudes were run for each of the sweeps. The results are presented in Figure 15. The maximum positive downrange divert and maximum crossrange divert are shown. The range achievable increases exponentially as the flight-path angle becomes more shallow.
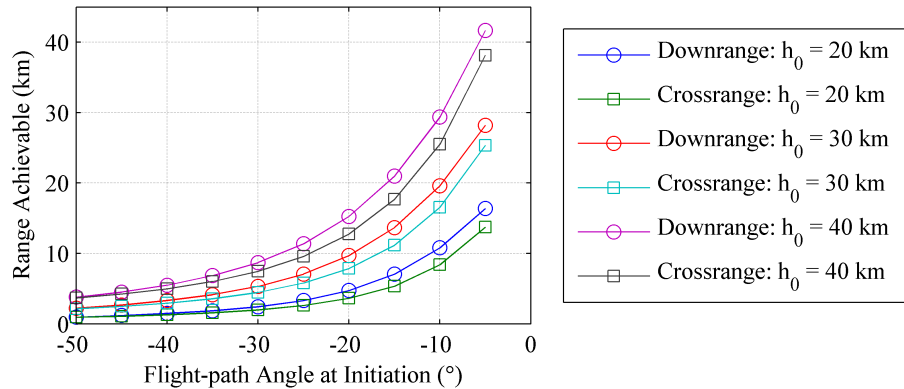

Figure 15. Range sensitivity to flight-path angle at initiation.

Although the trajectory is ballistic, shallower flight-path angles will allow the trajectory to naturally traverse more range and spend more time at higher altitudes so divert maneuvers will have greater range effects. If the flight-path angle is shallow enough, these maneuvers can actually cause the vehicle to loft (positive flight path angle) and maintain altitude for longer periods of time.

4. Thruster Size

On entry vehicles, thrusters have been used on the backshell for multiple purposes. For bank-to-steer applications, small reaction control thrusters apply torques on the vehicle to rotate the vehicle's lift vector. The MSL entry vehicle carried four pods of two RCS thrusters for a total thrust of about 580 N per pod, corresponding to a T/W = 0.05 when referenced to the MSL vehicle at Mars. RCS thrusters with such T/W are not typically used for translational thrusts and are ineffective in some aerodynamic regimes.[20] Another relevant flown application is the Transverse Impulse Rocket System (TIRS) from the Mars Exploration Rover,[21] which used a short-duration solid

13

rocket to arrest the horizontal velocity of the vehicle. This system was used for translational thrusts off to the side of the vehicle, much like the application conceptualized for this maneuver. The MLE's conceptualized for this baseline mission were used for deceleration and divert purposes and correspond to a T/W of about 0.5 for a pair of engines. Although not directly accounted for in this study, engine mass is linearly proportional to thrust, and higher thrust engines would require more massive engines (detracting from potential payload mass).[22]

Figure 16 shows the influence of thruster size on achievable positive downrange and crossrange, relative to an MSL class 3300 kg vehicle. Initation velocity was fixed at 800 m/s, and results for three different ballistic coefficients are presented, which is directly correlated to initation altitude. The range is limited by the time available for the maneuver, and smaller thrusts require more time to impart the same amount of ΔV on the trajectory. For higher ballistic coefficients, the relation for range achievable to T/W is approximately linear with some exponential characteristics for higher ballistic coefficients. Achievable crossrange is consistently 5-10 km less than downrange across the T/W space.
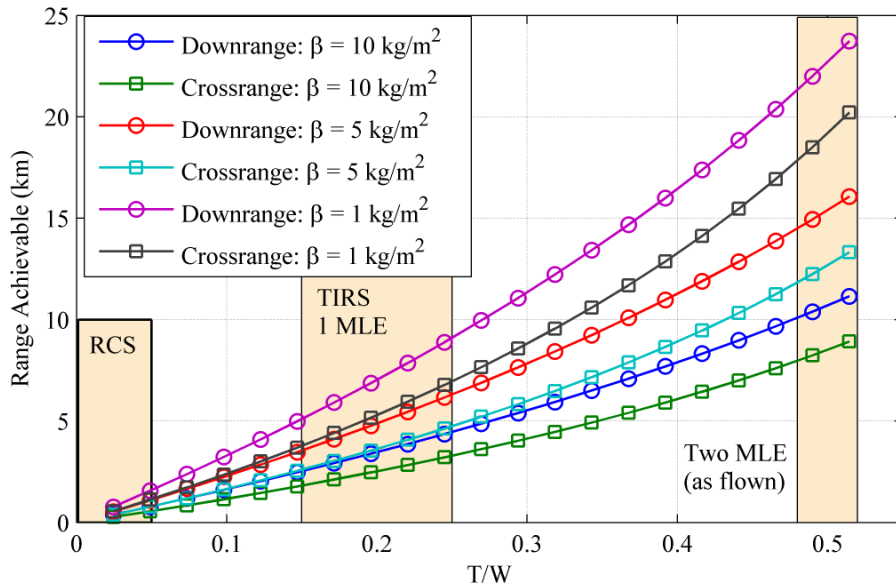

Figure 16. Range sensitivity to thruster size and ballistic coefficient at initiation.

IV. Supersonic Retropropulsion Divert Architecture

A. Conceptual Description

Past entry architectures that have conceptualized using supersonic retropropulsion use it purely as a decelerator in the supersonic regime. In this manner, thrust is applied directly against the velocity.[23] With precision landing becoming an increasingly more important requirement, it is postulated that performing divert maneuvers during this phase may be beneficial. Current state-of-the-art propulsive descent guidance use optimal control techniques to divert to a landing site. To date propulsive guidance has only been investigated in the subsonic flight regime[8] and current entry architectures have used supersonic retropropulsion only for deceleration. By expanding the start of propulsive descent guidance into the supersonic regime, both deceleration and a targeted divert can be achieved by supersonic retropropulsion. Using the results from the previously described architecture, it is postulated that diverts at higher velocities and altitudes will more efficiently use fuel to achieve landing goals. These diverts are accomplished with thrust vectoring during the supersonic phase of flight.

B. Architecture Detail

The vectored-thrust supersonic retropropulsion architecture is described in detail in Figure 17. The angle θ is defined as the off-velocity thrust angle, which can be constrained relative to the velocity vector that the thrust can vector, while the vehicle is supersonic. This is a practical constraint, similar to angle-of-attack, that is set by aerodynamic limitations (the vehicle is stable at certain angle-of-attacks, for example) and navigation sensor viewing constraints. Existing SRP studies assume propulsive gravity turn laws during the SRP burn, where $\theta = 0°$ throughout the entire trajectory.[4,24] For this architecture, when the vehicle passes into the subsonic regime, thrust vectoring is unconstrained until touchdown. If increased navigation accuracy is desired, the transition between hypersonic entry and SRP initiation may allow for the exposing of a TRN or radar sensor while the engines are being exposed.
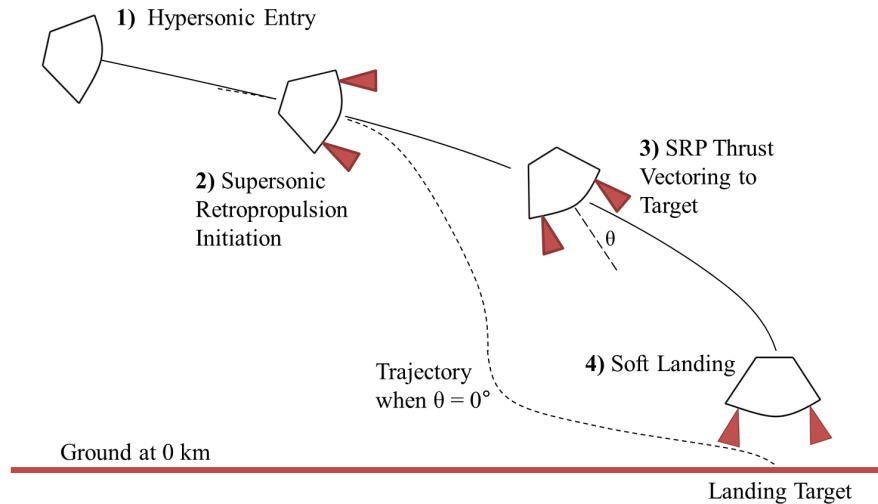

Figure 17. Architecture with thrust vectoring during SRP.

C. Supersonic Retropropulsion Guidance and Implementation Strategy

The optimal propulsive guidance law from the previous architecture study is used.[8,19] This is an analytic, acceleration-optimal guidance law, that uses a Lagrange multiplier approach to determine acceleration commands. At every guidance call, run at 10 Hz, the algorithm determines an acceleration vector. The optimal propulsive trajectory is verified within the algorithm to make sure that the trajectory is feasible (trajectory does not pass through the ground). If it is in violation, a weighting on time-to-go is increased, until the algorithm finds a trajectory that meets the constraints. The acceleration is constrained to the maximum and minimum thrust capability of the system. If the vehicle is supersonic, the off-velocity thrust angle is checked to make sure it satisfies a prescribed angle constraint. If it is exceeded, the thrust vector is rotated on the velocity-thrust vector plane to the angle constraint.

1. Glideslope constraint

A common feature of optimal propulsive descent trajectories is fast-moving, but low altitude flight. This often causes a >100 m/s glide a few hundred meters off the ground, often ending in a high-velocity impact during the simulation. In order to mitigate these events, a 20° glideslope constraint is applied when the vehicle is farther than 750 m away from the landing site.

This glideslope constraint is not handled by the optimal landing law, so a different propulsive landing law was used in this situation. At the point where the vehicle violates the glideslope, a trajectory based on a polynomial law is created towards the target. Since the vehicle cannot instaneously transition into this trajectory, a feedback linearization control law is used to allow the vehicle to safely transition and follow the new trajectory. Although not fuel-optimal, it is able to create flight-realistic trajectories.

2. Range Trigger (SRP Initiation Mach Number)

The guidance law is unable to determine a Mach number to initiate SRP. This is important, since it may be more efficient to initiate earlier or later, depending on how far downrange the target is relative to the vehicle. To account for this, the initiation Mach number is kept as a free variable in the simulation. A function for the propellant mass fraction is created, where PMF = f(SRP initiation Mach number). A golden-section search method is used to determine what initiation Mach number produces the minimum PMF. The initiation of SRP at this Mach number tends to act as a range trigger.[25]

D. Simulation Assumptions

Although the same simulation environment is used as the previous study, additional assumptions are made regarding thrust limitations and aerodynamics. Minimum thrust is constrained to 10% of maximum thrust, reflecting deep throttling capabilities. Also, the thrust vector is allowed to change direction instantaneously. This assumption was found to be valid because the tested trajectories usually had continuous thrust movement, except when the thrust angle constraint is changed during flight. When the vehicle is supersonic, the off-velocity thrust angle is limited to a prescribed angle (effectively angle-of-attack), but as soon as the vehicle is subsonic, this angle is unconstrained. Aerodynamic forces are ignored while the vehicle is thrusting, except when otherwise stated for aerodynamic drag preservation studies.

E. Architecture Performance

1. Vehicle Description

In an effort to understand results of the maneuver, a modified Mars Science Laboratory[26] vehicle is simulated. This vehicle is shown in Figure 18. A modified Apollo Final Phase guidance algorithm is used for hypersonic entry, and produces a constant altitude segment between 10 and 20 km, much like was seen in the MSL mission. Methane – LOx engines are used for parity with previous studies.[4] The engines are assumed to be fixed at 0° cant, with thrust vectoring achieved through the use of differential throttling.

Table 9. Vehicle parameters for the SRP thrust vectoring study.

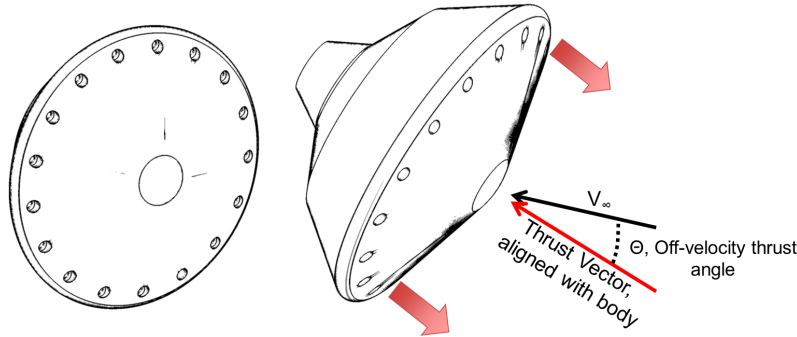| Vehicle Parameter		Value
Mass		3300 kg
Aerodynamics	Aeroshell	70° sphere-cone, 4.5 m diameter
	L/D	0.24
Engine	T/W (Mars-relative, at start)	5 (~17 MLEs at 0° cant)
	Propellant (Isp (s))	Methane – LOX (350 s)

Figure 18. Configuration conceptualized for use in the SRP study.

2. Achievable Performance

Achievable range on contours of PMF are analyzed for the MSL type vehicle in Figure 19, at different supersonic off-velocity thrust angle constraints. On the left of each of the plots is the fully constrained 0° thrust angle, representative of the traditional architecture.[4]

As the thrust angle constraint is relaxed, less fuel is necessary to perform larger diverts. The largest improvement is seen in positive downrange diverts, and the least is seen in negative downrange diverts. Negative downrange diverts likely do not see too much improvement since a range trigger (irrespective of thrust vectoring) begins the retropropulsion burn earlier to target the site. Positive downrange diverts see an improvement with thrust vectoring, since a larger off-velocity thrust angle can allow thrust to more easily counteract gravity, and provide the timeline and altitude margin necessary to carry the vehicle further downrange. For a +10 km downrange and +5 km crossrange divert, a 0° constrained trajectory requires a PMF a little over 0.3, while the unconstrained trajectory requires a PMF of about 0.15, roughly a 50% reduction in PMF.
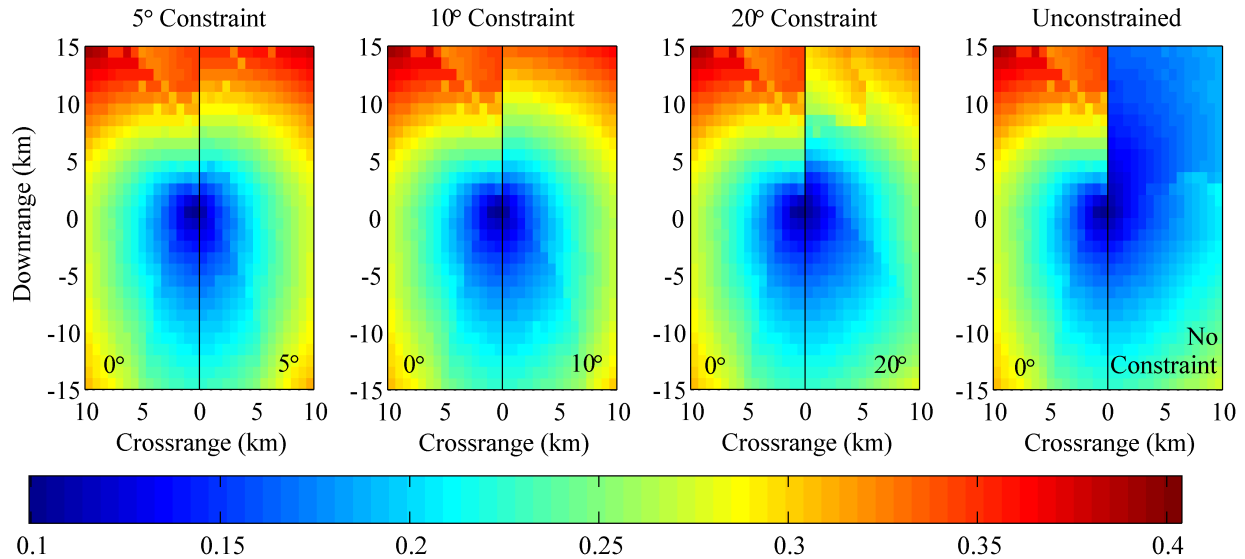

Figure 19. Range achievable on contours of PMF, for different supersonic off-velocity thrust angles. The left side of each plot shows the 0° constraint contour for comparison, while the right shows the contour for the titled constraint.

3. Sensitivity to Initial Conditions

An architecture that lands only with a propulsive constant-thrust gravity turn law is initially swept in initial altitude and flight-path angle to understand nominal sensitivities to initial conditions. A parameter sweep is run from an altitude of 500 m to 20 km, and flight-path angles of 5° to -45°. Positive flight path angles represent a loft in the trajectory (lifting vehicle). Initiation velocity is varied with a linear relationship where $V_0 = 350$ m/s at 0 km altitude, and 750 m/s at 20 km altitude to account for terminal velocity differences at different altitudes. If the vehicle lands at a velocity greater than 25 m/s, the initial conditions are treated as infeasible, and the solution is rejected (T/W limited to 5). The resulting PMF with MSL and Pathfinder trajectories are shown in Figure 20.

Figure 20. Sensitivity of initial altitude and flight-path angle on contours of PMF for a gravity turn. MSL (solid) and Pathfinder (dashed) trajectories are overlaid.

The PMF required to perform a gravity turn to the ground decreases when flight-path angle approaches zero, and altitude is as low as possible. As initiation altitude decreases, less fuel is required, due to the fact that there is less time for gravity losses to act on the vehicle. When flight-path angle is near 0°, PMF also decreases since the vehicle traverses range at a quicker rate. Also, as flight path angle increases towards the positive, a lower altitude

initiation becomes more and more feasible. It is preferred to limit vertical velocity as close to zero as possible near the ground, and large downward velocities due to steep flight-path angles. make it difficult to slow down and land softly.

Superimposed on Figure 20 are simulated trajectories of Pathfinder (dashed) and MSL (solid). The MSL trajectory includes a loft. A higher ballistic coefficient body would be able to retain a shallower flight path angle into lower altitudes, falling to the left of the MSL trajectory, and therefore reducing PMF required. A higher lift body (like an ellipsled) would also be able to keep a shallow flight path angle or actually loft at lower altitudes, also falling to the left of the MSL trajectory. Pathfinder was a ballistic entry with a $\beta = 62.4$ kg/m^2, and a lower β vehicle would likely fall to the right of this line. Overall, to minimize PMF, it would be beneficial to initiate SRP at as low of an altitude as possible, while maintaining a shallow flight path angle, and maybe even a minor loft, as evident in Figure 20. A lifting, high ballistic coefficient vehicle may be effective in achieving this goal.

Since most benefit in PMF (as seen in Figure 19) occur for downrange diverts, the PMF required to perform a 10 km positive downrange divert is investigated for the same range of initial conditions. A 10 km downrange divert would also represent a likely divert given the 20 km x 10 km landing ellipse of the MSL mission. Initial altitude, velocity, and flight-path angle are varied at simulation start. Simulation start is not necessarily SRP start, since the range trigger guidance approach chooses when to initiate SRP. The results of this sweep are seen in Figure 21, for 0°, 10°, 20° and unconstrained supersonic off-velocity thrust angle.
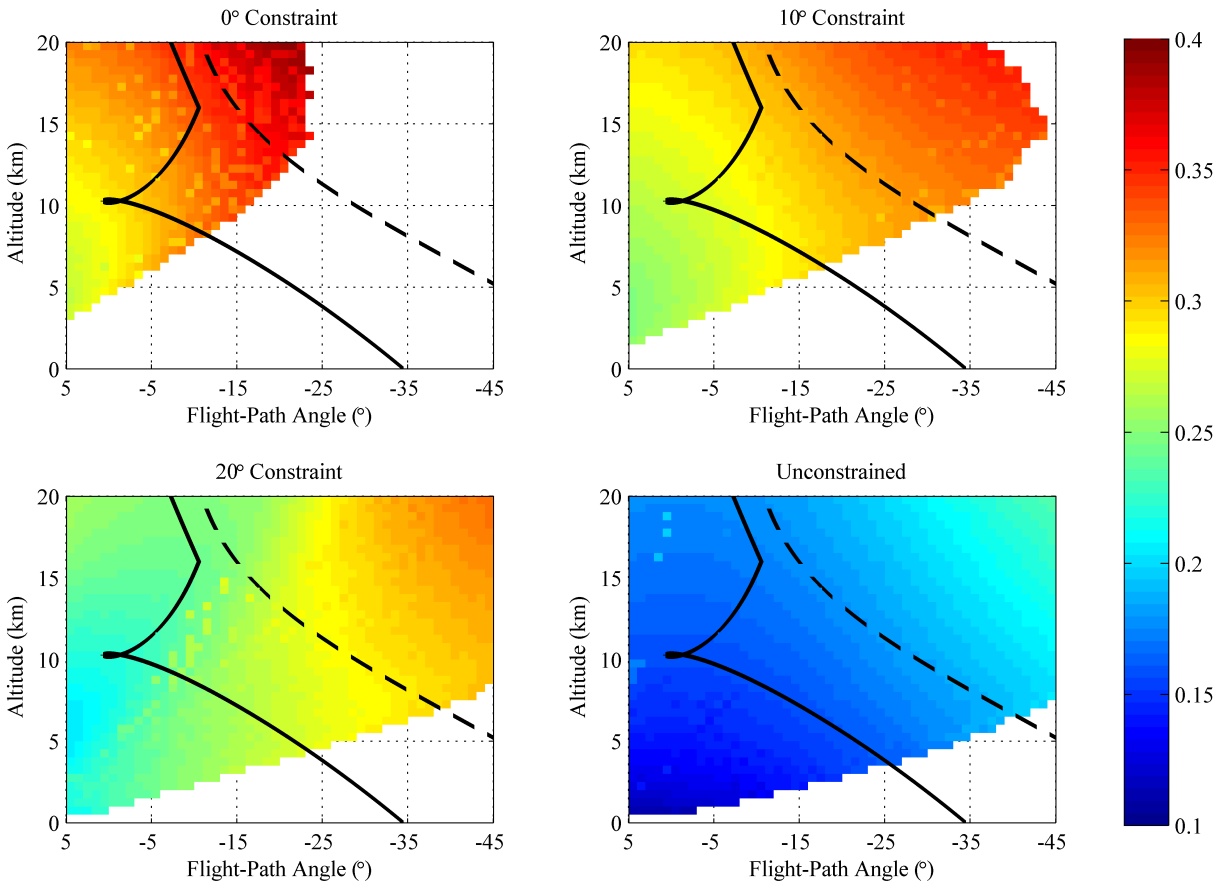

Figure 21. Altitude vs. flight-path angle sensitivity in PMF for trajectories requiring a 10 km downrange divert, separated by maximum supersonic off-velocity thrust angle.

For the fully constrained supersonic thrust angle (0°) cases, a 10 km positive downrange divert is only possible if the altitude and flight path angle are limited to the altitudes and flight-path angles shown in the plot. As the constraint opens up, lower altitudes and steeper flight path angles are able to complete the divert, and the divert only becomes limited by altitude at initiation at higher thrust angle constraints. As expected, propellant mass fraction generally decreases as the thrust angle constraint is relaxed.

To further show how relaxing the thrust angle constraint decreases PMF required, the percent difference in PMF for the different thrust angle constraints compared to the 0° constraint is calculated and reported in Figure 22. Since the 0° case does not have PMF data for all altitudes and flight-path angles, the comparison is constrained to those initial conditions. For the 10°, 20°, and unconstrained cases, PMF is reduced by at least 10%, 20%, and 40%, respectively, regardless of the initial conditions. These performance gains are for a 10 km divert, reflecting the scenario where the most reduction in PMF would be seen with thrust vectoring.
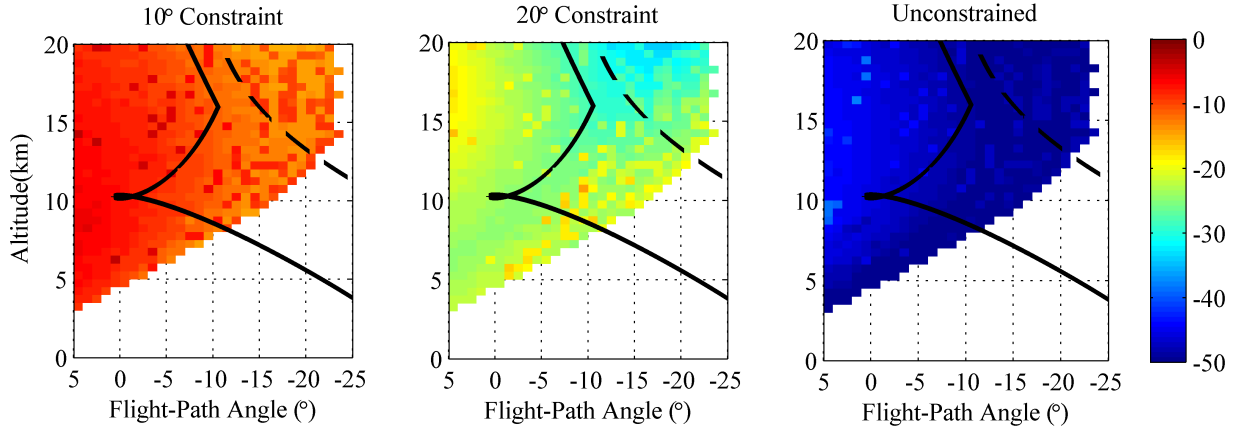

Figure 22. Contours of percent reduction in PMF for 10°, 20°, and unconstrained trajectories relative to the 0° trajectory

4. Other Considerations

Initiation velocity is a difficult trend to analyze, but due to the short burn times of the maneuver, the ideal rocket equation serves as a good estimate for the propellant mass fraction. Also, it would be preferred to let the vehicle choose the initiation velocity in-flight that can best accomplish a divert.

Engine operating conditions and acceleration limitations can guide the selection of the thrust-to-weight for the engine. If the rocket engine is designed for minimal restarts and has a constrained operating regime, it may be best to choose the thrust-to-weight based on the requirements for those given missions. Likewise, for a Human mission, deceleration constraints will likely come into play and prevent bang-off-bang optimal trajectories.

F. Statistical Performance

One-thousand runs were performed with appropriate dispersions as found in Table 4, for differing supersonic thrust angle constraints. A single landing target was chosen, based on the center of a landing ellipse of the unguided trajectories. The supersonic thrust angle constraint was varied: 0°, representing a traditional architecture where thrust directly opposes velocity, 10°, 20°, and unconstrained.

1. Propellant Mass Fraction and Miss Distance

Propellant mass fraction and miss distance are reported in cumulative distribution functions in Figure 23, with 99% CI PMF figures in Table 10. Across the board, PMF is decreased as the thrust angle constraint is relaxed, with up to a 32% reduction for the unconstrained case. As the vehicle thrust angle constraint is relaxed, the vehicle is allowed to follow more optimal trajectories, and thus the divert can be handled with less fuel. Although a 10% reduction might be modest for the 10° case, it could amount to few hundred kilograms on large vehicles. This supports the PMF reductions found in the sensitivity studies. Likewise, miss distance at the 99% CI is kept between 50-90 m.

Table 10. 99% confidence for PMF from the Monte Carlo runs.

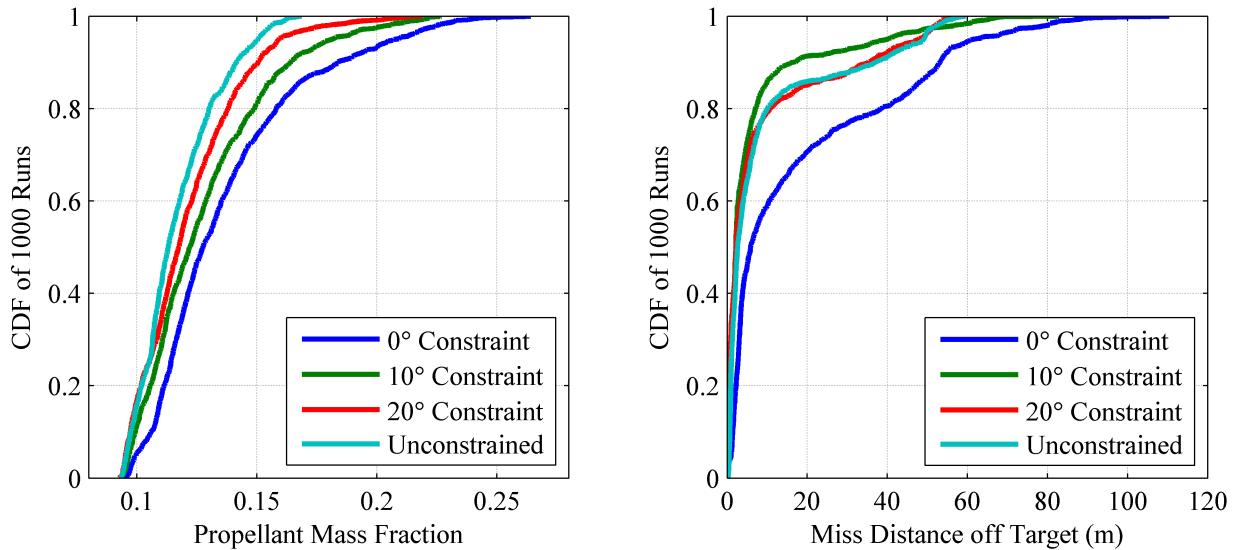|	0° (Traditional)	10°	20°	Unconstrained
99% PMF	0.233	0.214 (10% reduction)	0.199 (16.4% reduction)	0.161 (32.3% reduction)

19

Figure 23. CDF's of PMF (left) and miss distance (right) for Monte Carlo runs with different thrust angle constraints.

Statistics of landing velocity and Mach number at SRP initiation are documented in Figure 24. All cases demonstrate soft landing capability, with all landings under 25 m/s. The deceleration from 25 m/s to 0 m/s can happen quickly with the thrust-to-weight of the baseline vehicle design. The knee at 2 and 5 m/s indicate the trajectories that violated a glideslope constraint, and were forced to follow a polynomial law. Initiation Mach number does not differ much between constraints, except that the unconstrained cases initiate at a slightly lower Mach number. Initiation occurs between Mach 1.3 and 2.1 and is indicative of the golden-search method at work to choose the minimum fuel initation Mach number.
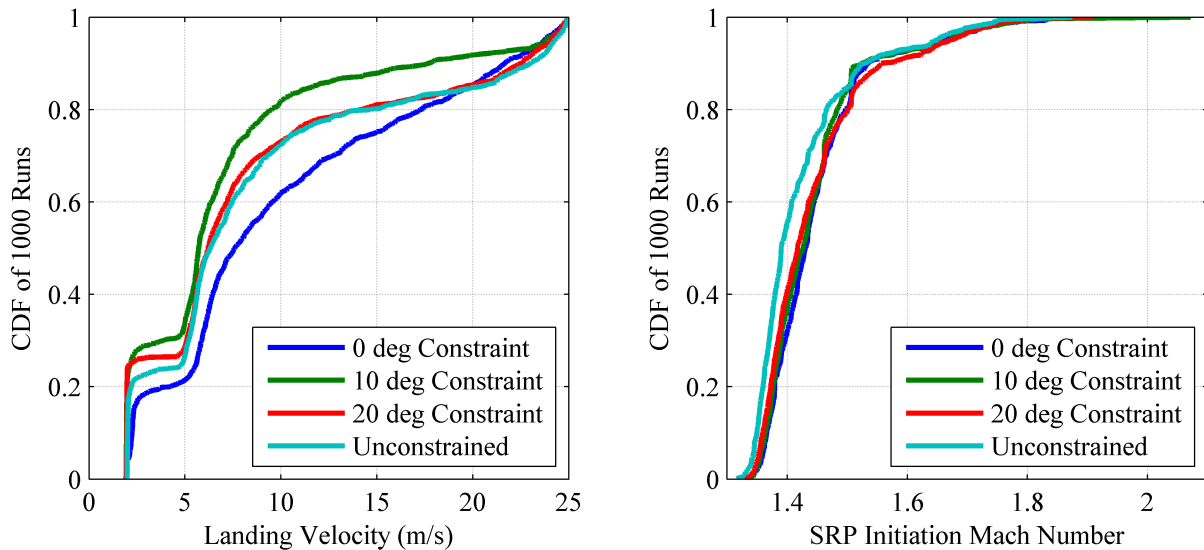

Figure 24. CDF's of landing velocity (left) and SRP initation Mach number for the Monte Carlo runs.

To better understand the trajectories, altitude verse downrange for each of the 1000 trajectories is plotted in Figure 25 for different supersonic thrust angle constraints. As expected, vehicles that need a larger divert (near the extremes of the trajectory), initiate earlier (and hence higher in altitude) compared to the vehicles in the center.
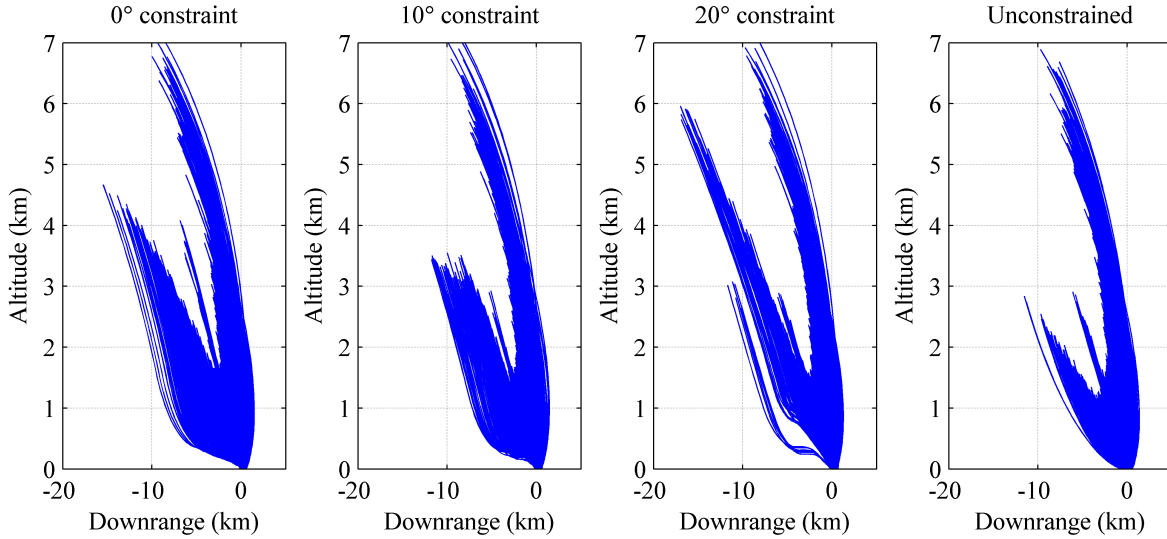
Figure 25. Altitude vs. downrange from the Monte Carlo runs for different supersonic thrust angle constraints.

For the trajectories that need to travel further downrange (the trajectories that are the furthest left on the plot), a glideslope constraint is hit, and the trajectory is forced to hold the glideslope while traveling to the target. Trajectories that need to travel back uprange (trajectories that are furthest right on the plot) do not exhibit this behavior, but rather the burn is initiated early and at higher altitudes in order to prevent the vehicle from traveling too far downrange. Likewise, the effect of the thrust angle constraints can be seen. The more constrained cases follow a straight trajectory in the high altitudes, with large corrections near the end of the trajectory, while the unconstrained cases follow a more fluid trajectory towards the target. The trajectories in the middle that initiate at higher altitudes than other middle trajectories indicate crossrange diverts.

Figure 26 shows the thrust angle behavior throughout supersonic flight. This figure demonstrates that the thrust constraint is active for some of the trajectories. Note for the 0° constrained cases, the 0.16° maximum is within an acceptable tolerance of the constraint. For a few of the unconstrained large diverts, an 80° initial thrust angle may be necessary, but it decreases to about 40° when crossing Mach 1. After initiation, thrust angle does not change much which means quick maneuvers are not required for diverts during supersonic retropropulsion. Also of interest is the fact that no trajectories favor a 0° thrust angle.
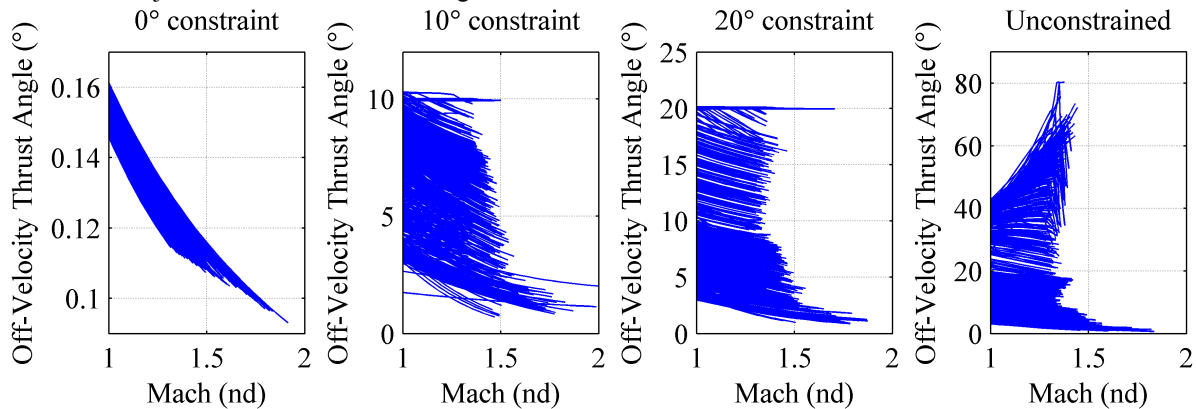

Figure 26. Thrust angle vs. Mach from the Monte Carlo runs for different supersonic thrust angle constraints.

The thrust coefficient, C_T, defined as $T / (q_\infty A)$,[23] is useful in defining aerodynamic regimes where drag preservation may exist. The C_T vs. Mach curves for all trajectories can be found in Figure 27. All the trajectories show that thrust coefficients range between 1 and 15 for all trajectories.
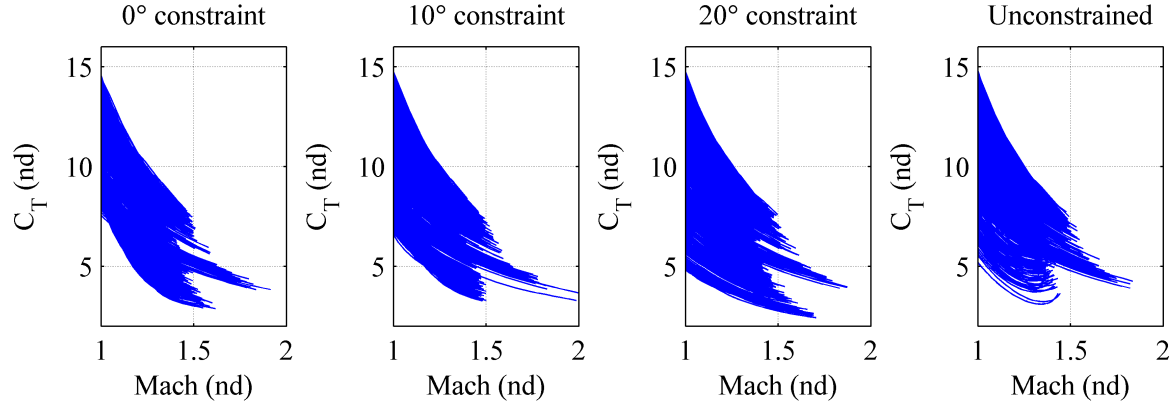
Figure 27. C_T vs. Mach from the Monte Carlo runs for different supersonic thrust angle constraints.

G. Aerodynamic Drag Preservation

Cordell has been able to show full aerodynamic preservation for C_T's up to 20 in configurations with six nozzles spaced around the aftbody with nozzle cant at 30°.[27] Such a configuration is appropriate for this study since C_T values between 2 and 15 are encountered during this trajectory. This drag model was implemented in the simulator and SRP at an off-velocity thrust angle of 0° was simulated. Three configurations were run, the 0° constrained with no aerodynamics, a 0° constrained with full drag preservation and nozzle cant at 30°, and a 0° constrained with full drag preservation and nozzle cant at 0° (represents a fictitious best case). The PMF CDFs are found in Figure 28, and the 99% CI PMF are found in Table 11. The cant angle 0° solutions provide a fair comparison between having and not having aerodynamic drag preservation. Aerodynamic drag preservation improves performance by almost 10% (0.213 vs. 0.233) at the 99% CI. However, the cant angle 0° with aerodynamic drag preservation serves as a fictitious best case, and when including cant angle cosine losses, performance worsens by 5% compared to the case without aerodynamic influences.
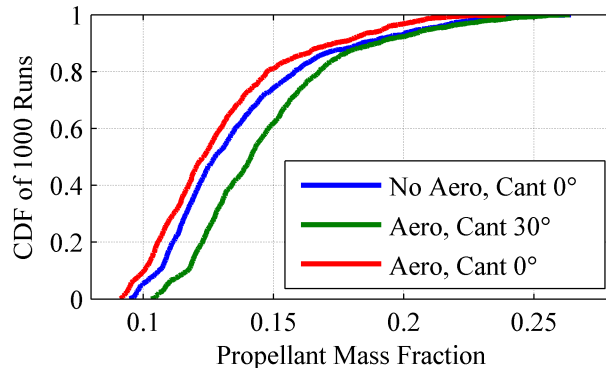

Figure 28. PMF CDF for Aerodynamic Drag Preservation Study.

Table 11. 99% CI PMF for Aerodynamic Drag Preservation Study.

	99% CI PMF
No Aero, Cant 0°	0.233
Aero, Cant 30°	0.243
Aero, Cant 0°	0.213

The contributions of the thrust and drag for deceleration throughout the supersonic regime can be found in Figure 29, for the 30˚ cant case with aerodynamic drag preservation. The thrust and drag forces were averaged out over the 1000 runs to see the trends in the supersonic regime. For the trajectories tested, drag provides about 20-30% of total deceleration across the regime. The trends indicate that the contribution of drag to total deceleration may increase at higher Mach numbers (highest initation Mach Number with these missions is Mach 1.9). Drag is significant and performance would likely increase with a drag preserved configuration even into the subsonic regime. However, it is important to minimize cosine losses while preserving aerodynamic drag in future configurations in order to capitalize on the aerodynamic gains. Even more gains can be had if thrust vectoring is allowed during flight as seen in Table 10.
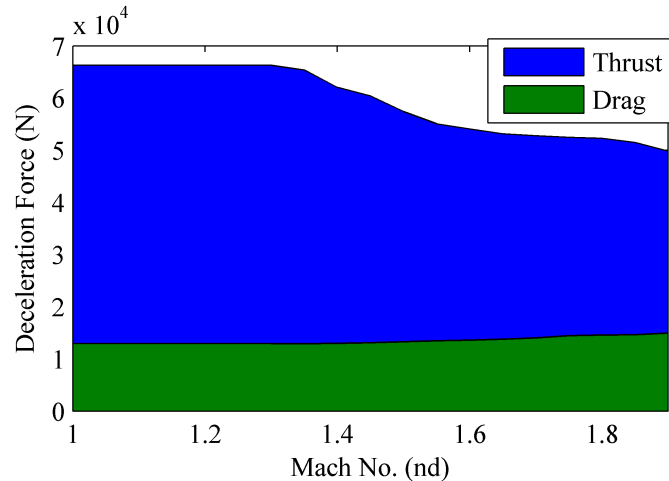
Figure 29. Contributions of thrust and drag through the supersonic regime, averaged out over 1000 runs, for the 30° cant case with aerodynamic drag preservation.

V. Conclusions

Two new architectures that utilize supersonic propulsive divert maneuvers have been presented. One is the high-altitude divert maneuver, which leverages altitude margin of low ballistic coefficient vehicles to perform diverts to a target, while the other involves thrust vectoring during supersonic retropropulsion. Expanding the propulsive maneuver envelope into the supersonic regime has been shown to have benefits in both range control and propellant usage efficiency.

The high-altitude divert maneuver was found to enable landing within 500 m for vehicles that enter on a ballistic trajectory with hypersonic $\beta \leq 10$ kg/m^2, without the need for entry guidance. This architecture is over 37% more efficient in propellant mass fraction compared to state-of-the-art propulsive landing architures. This architecture is most sensitive to flight-path angle at initiation, where very shallow flight-path angles dramatically improve achievable range. Likewise, since the maneuver is timeline constrained, thrust-to-weight is also important in making sure enough ΔV is imparted to achieve the divert in the given time. Missions that utilize low ballistic coefficient vehicles may benefit from this architecture to decrease landing error.

Thrust vectoring during supersonic retropropulsion was found to save fuel while achieving pinpoint landing goals. Traditional SRP architectures have utilized thrusts directly opposing the velocity vector, but if the supersonic off-velocity thrust angle is relaxed, savings in propellant mass fraction over 30% are possible, with no loss in landing precision. Initiating SRP at low altitudes and shallow flight-path angles was shown to be benefical in terms of propellant usage. Aerodynamic drag preservation can improve propellant by up to 10% in the best case, and tied in with thrust vectoring, this can have a substantial effect in reducing the propellant use in future architectures.

VI. Acknowledgments

VII. References

[1] Braun, R. D. and Manning, R. M., "Mars Exploration Entry, Descent, and Landing Challenges," Journal of Spacecraft and Rockets, Vol. 44, No. 2, 2007, pp. 310-323.

[2] Dwyer-Cianciolo, A. M., Davis, J. L., Komar, D. R., Munk, M. M., Samareh, J. A., Powell, R. W., Shidner, J. D., Stanley, D. O., Wilhite, A. W., Kinney, D. J., McGuire, M. K., Arnold, J. O., Howard, A. R., Sostaric, R. R., Studak, J. W., Zumwalt, C. H., Llama, E. G., Casoliva, J., Ivanov, M. C., Clark, I., and Sengupta, A., "Entry, Descent and Landing Systems Analysis Study: Phase 1 Report," Tech. Rep. TM-2010-216720, NASA, July 2010.

[3] Drake, B. G., ed., "Human Exploration of Mars: Design Reference Architecture 5.0", NASA-SP-2009-566, 2009.

[4] Steinfeldt, B., Theisinger, J., Korzun, A., Clark, I., Grant, M., and Braun, R., "High Mass Mars Entry, Descent, and Landing Architecture Assessment," AIAA 2009-6684, AIAA Space 2009 Conference and Exposition, Pasadena, CA, 14-17 Sept. 2009.

[5] Mendeck, G. F. and Craig, L. E., "Entry Guidance for the 2011 Mars Science Laboratory mission," AIAA 2011-6639, Portland, OR, Aug. 2011.

[6] Açikmeşe, B., and Ploen, S., "Convex Programming Approach to Powered Descent Guidance for Mars Landing," Journal of Guidance, Control, and Dynamics, Vol. 30, No. 5, pp. 1353-1366, 2007.

[7] Wolf, A.A.; Tooley, J.; Ploen, S.; Ivanov, M.; Acikmese, B.; Gromov, K., "Performance Trades for Mars pinpoint Landing," *IEEE Aerospace Conference, 2006.*

[8] Steinfeldt, B.A.; Grant, M.J.; Matz, D.A.; Braun, R.D.; and Barton, G.; "Guidance Navigation and Control System Performance Trades for Mars Pinpoint Landing,"*Journal of Spacecraft and Rockets*, Vol. 47, No. 1, pp. 188-198, Jan-Feb, 2010.

[9] Meginnis, I.M.; Putnam, Z.R.; Clark, I.G.; Braun, R.D.; and Barton, G.H.; "Guided Entry Performance of Low Ballistic Coefficient Vehicles at Mars," *Journal of Spacecraft and Rockets*, Vol. 50, No. 5, pp. 1047-1059, Sept-Oct, 2013.

[10] Grant, M.J., et al., "Smart Divert: A New Mars Robotic Entry, Descent, and Landing Architecture," *Journal of Spacecraft and Rockets*, Vol. 47, pp. 385-393, May-June 2010.

[11] Davis, J.L., Shidner, J.D., Way, D.W., "Mars Science Laboratory Post-Landing Location Estimation Using POST2 Trajectory Simulation," AAS 13-313, 23rd AAS/AIAA Spaceflight Mechanics Meeting, Kauai, HI, February 2013.

[12] Johnson, A.E., Bergh, C., Chang, Y., et al., "Design and Ground Test Results for the Lander Vision System," AAS 13-042, 36th Annual AAS Guidance & Control Conference, Breckenridge, CO, February 2013.

[13] Pastor, P.R., Gay, R.S., Striepe, S.A., Bishop, R.H., "Mars Entry Navigation from EKF Processing of Beacon Data," AIAA 2000-4426, Astrodynamics Specialist Conference, 2000.

[14] H. L. Justh and H. S. Ramey, "MARS-GRAM 2010: IMPROVING THE PRECISION OF MARSGRAM,"
4th InternationalWorkshop on the Mars Atmosphere: Modelling and Observations, Feb. 2011,
pp. 1–4.

[15] Cruz, J.R., et al., "Parachute Models Used in the Mars Science Laboratory Entry, Descent, and Landing Simulation," AIAA 2013-1276, 2013 AIAA Aerodynamic Decelerator Systems Conference, March 2013.

[16] Putnam, Z.R. and Braun, R.D.; "Precision Landing at Mars Using Discrete-event Drag Modulation," AAS-13-438, 23rd AAS/AIAA Spaceflight Mechanics Meeting, Kauai, HI, February 2013.

[17] Prakash, R., Burkhart, P. D., Chen, A., *et al.* "Mars Science Laboratory Entry, Descent, and Landing System Overview". 2008 IEEE Aerospace Conference. Big Sky, Montana. pp. 1–18.

[18] Clark, I.M., Hutchings, A.L., Tanner, C.L., and Braun, R.D. "Supersonic Inflatable Aerodynamic Decelerators for Use on Future Robotic Missions to Mars," *Journal of Spacecraft and Rockets*, Vol. 46, No. 2, pp. 340-352, Mar-Apr, 2009.

[19] D'Souza, C., "An Optimal Guidance Law for Planetary Landing," AIAA Guidance, Navigation, and Control Conference, AIAA Paper 97-3709, Aug. 1997.

[20] Dyakonov, A.A., Glass, C.E., Desai, P.N., Van Norman J.W. "Analysis of Effectiveness of Phoenix Entry Reaction Control System," *Journal of Spacecraft and Rockets*, Vol. 48, No. 5 (2011), pp.746-755.

[21] San Martin, A.M., Bailey, E. "The Mars Exploration Rover (MER) Transverse Impulse Rocket System (TIRS)," 2005 AAS Guidance and Control Conference, Breckenride, Colorado.

[22] Christian, J.; Manyapu, K.; Wells, G.; Lafleur, J.; Verges, A.; and Braun, R.; "Sizing of an Entry, Descent, and Landing System for Human Mars Exploration," AIAA 2006-7427, AIAA Space 2006 Conference and Exposition, San Jose, CA, September 2006.

[23] Korzun, A.M., Braun, R.D., "Performance Characterization of Supersonic Retropropulsion for High-Mass Mars Entry Systems," *Journal of Spacecraft and Rockets*, Vol. 47, No. 5, pp. 836-848, Sep.-Oct., 2010.

[24] Marsh, C.L. and Braun, R.D.; "Fully Propulsive Mars Atmospheric Transit Strategies for High-Mass Missions," *Journal of Spacecraft and Rockets*, Vol. 48, No. 2, pp. 271-282, Mar-Apr, 2011.

[25] Wolf, A., Ivanov, M., "SuperSmart Parachute Deployment Algorithm for Mars Pinpoint Landing," AIAA/AAS Astrodynamics Specialist Conference and Exhibit, 2008.

[26] Prakash, R., Burkhart, P. D., Chen, A., *et al.* "Mars Science Laboratory Entry, Descent, and Landing System Overview". 2008 IEEE Aerospace Conference. Big Sky, Montana. pp. 1–18.

[27] Cordell, C., "Configuration Based Computational Fluid Dynamics and Analytical Modeling of Supersonic Retropropulsion Flow Field Structures," Ph.D. Thesis, Georgia Insitute of Technology, 2013.